Self-Powered Multiinput Hybrid Rectifier With Arbitrary Phase Difference and Low Start-Up Voltage for Piezoelectric Energy Harvesting

Jiaming Xiong, Yinshui Xia, Zhidong Chen, Huakang Xia, and Changjian Xiao

***Abstract*—Harvesting vibration energy from multiple piezoelectric transducers (PZTs) can significantly enhance output power. However, prevailing methods either employ time-division multiplexing of the inductor to harvest energy or rely on complex external circuits to control switches, resulting in low energy conversion efficiency. A self-powered multi-input hybrid rectifier (SP-MIHR) with arbitrary phase difference and low start-up voltage is proposed in this article. There are both voltage bias flip and series synchronous switch harvesting on inductor (S-SSHI) operating modes, enabling energy harvesting from multiple PZTs with arbitrary phase difference using a single inductor. Experimental results show that the SP-MIHR circuit has a maximum end-to-end energy conversion efficiency of 67.3% and a maximum output power that is 1.47 times higher than that of the classical S-SSHI circuit, with a start-up voltage that is 0.5 V lower than that of the S-SSHI circuit. Compared with the multi-input standard energy harvesting circuit, the SP-MIHR circuit can achieve 4.12× power improvement and 1.3× voltage improvement with a simple structure and excellent scalability for multiple PZTs energy harvesting.**

***Index Terms*—Hybrid rectifier, multi-input interface, piezoelectric energy harvesting (EH), self-powered, series synchronous switch harvesting on inductor (S-SSHI).**

I. INTRODUCTION

WITH the continuous advancement of Internet of Things technology and wireless communication technology, wireless sensor networks (WSNs) have been widely employed in areas of society, including smart cities, environmental monitoring, telemedicine, and beyond [1]. However, the long-term operation of WSN nodes is limited by sustainable energy supply. Traditional methods utilizing batteries or wired power sources not only contribute to environmental pollution but also face limitations in terms of time and spatial scales. Hence, converting environmental energy into electrical energy to power WSN nodes has emerged as an effective solution to address this challenge [2].

The environmental energy that can be collected includes vibration energy, solar energy, and thermal energy. Among them, vibration energy is widely distributed in nature and has a high energy density, which has attracted the attention of researchers [3]. Piezoelectric transducers (PZTs) use the piezoelectric effect of piezoelectric materials to convert mechanical energy resulting from vibrations into electrical energy [4]. However, the current produced by PZT is in the form of an alternating current, whereas the terminal load typically requires a stable direct current. To address this, an interface circuit with rectification, voltage stabilization, and impedance matching capabilities is essential for bridging the gap between the PZT and the terminal load [5].

The simplest interface circuit is the standard energy harvesting (SEH) circuit [6], which requires only four diodes and a filter capacitor. Although the structure of the SEH circuit is simple, the conduction voltage of the diodes results in large power losses. Moreover, due to the existence of parasitic capacitor in the PZT, there is a phase difference between current and voltage, resulting in a low energy harvesting (EH) efficiency of the SEH circuit [7].

To improve the energy conversion efficiency of the EH circuits, researchers have proposed a series of nonlinear EH interfaces. Lefeuvre et al. [8], [9] proposed series synchronous switch harvesting on inductor (S-SSHI) circuit and parallel synchronous switch harvesting on inductor (P-SSHI) circuit, collectively referred to as synchronous switch harvesting on inductor (SSHI) circuit. The SSHI circuit enhances the EH efficiency of the interface circuit by flipping the voltage of the PZT, thereby synchronizing the phase of the voltage and current of the PZT. However, the EH efficiency of these two circuits is strongly influenced by the load. In order to eliminate the dependence of the interface circuit on the load, Lefeuvre et al. [10] proposed a synchronous electric charge extraction (SECE) circuit. The SECE circuit divides the energy extraction and storage into two steps. By decoupling the load side from

Received 2 April 2024; revised 19 July 2024 and 22 September 2024; accepted 9 November 2024. Date of publication 13 November 2024; date of current version 26 December 2024. This work was supported in part by the National Natural Science Foundation of China under Grant U22A2013 and Grant 62131010 and in part by the Natural Science Foundation of Zhejiang Province under Grant LR22F010001 and Grant LY21F010006. Recommended for publication by Associate Editor G.-S. Seo. *(Corresponding author: Yinshui Xia.)*

Jiaming Xiong, Yinshui Xia, Huakang Xia, and Changjian Xiao are with the Department of Electrical Engineering and Computer Science, Ningbo University, Ningbo 315211, China (e-mail: 2111082310@nbu.edu.cn; xiayinshui@nbu.edu.cn; xiahuakang@nbu.edu.cn; 2111082309@nbu.edu.cn).

Zhidong Chen is with the College of Information and Intelligence Engineering, Zhejiang Wanli University, Ningbo 315100, China (e-mail: 1701082016@nbu.edu.cn).

Color versions of one or more figures in this article are available at https://doi.org/10.1109/TPEL.2024.3497940.

Digital Object Identifier 10.1109/TPEL.2024.3497940

the front-end rectifier circuit, the output power of the PZT is independent of the load [11]. Similarly, maximum power point tracking (MPPT) technology can also be used to address the load dependency of the circuit [12]. Li et al. [13] used a disturbance observation algorithm to track the maximum power of the P-SSHI circuit, which improves the efficiency of the EH and reduces the load dependence of the circuit.

In order to further enhance the efficiency of EH, researchers continually refine circuit designs based on SSHI and SECE topologies. Sanchez et al. [14] proposed a P-SSHI circuit for periodic impulse excitation, while Dini et al. [15] proposed a SECE circuit with residual charge reversal. These circuits require precise switching control, but the additional control circuits consume power. In order to solve the problem of self-power supply for control switching, Liang et al. [16] proposed a self-powered S-SSHI circuit, while Shi et al. [17] presented a self-powered efficient SECE circuit. These circuits are controlled by passive peak detection (PKD) switches, which realize self-power supply, reduce circuit loss, and improve the efficiency of the EH. In recent years, some researchers devoted themselves to the research of hybrid rectifiers. Xia et al. [18] proposed a self-powered S-SSHI and SECE hybrid rectifier, which achieves the balance between the rectifier peak output power and the optimal rectifier voltage range. Lallart [19] proposed a series and P-SSHI circuit with high output power in a wide load range. However, two large inductors are used in these two circuits, which increases the size of the circuit and presents challenges to scalability.

The energy harvested by a single PZT is limited and hard to meet practical power supply requirements for loads. Hence, the study of multiple PZTs for the EH has garnered attention. Shareef et al. [20], Boisseau et al. [21], and Meng et al. [22] improved the SECE topology and implemented multiple PZTs interfaces of the SECE framework. However, these three circuits are all realized by the time-division multiplexing (TDM) of the inductor, precluding the simultaneous EH of multiple PZTs. To solve this problem, many researchers made constant efforts in the circuit structure optimization. Chen et al. [23] proposed a multi-input S-SSHI circuit, which uses two synchronous switches to eliminate the diode bridge rectifier and increase the output power, but the number of switches increases multiplicatively with the expansion of the number of PZTs. Long et al. [24] improved the P-SSHI circuit and realized the multi-input of PZTs but used two inductors, resulting in a bulky circuit. Wang et al. [25] proposed a multi-input SECE circuit based on the buck structure, which has a wide output voltage range but at the expense of reduced power output. Long et al. [26] proposed a multi-input ReL-SSHI circuit with MPPT, which realized the combination of PZT arrays EH and MPPT technology, thus improving the EH efficiency. However, only the inductor can be shared. The above-mentioned circuits have addressed the issue of charge cancellation endemic in traditional TDM designs, while they still have some deficiencies in circuit structure and output power.

In view of the above problems, a self-powered multi-input hybrid rectifier (SP-MIHR) is proposed in this article. The proposed SP-MIHR circuit employs an RC differential (RCD) circuit and PKD to control the switch, which effectively removes the full-bridge rectifier (FBR) in the traditional S-SSHI circuit. This design not only reduces the start-up voltage of the circuit, but also enhances the efficiency of EH by implementing a series-parallel hybrid inductor configuration. In addition, the SP-MIHR circuit can harvest energy from multiple PZTs with arbitrary phase differences using a single inductor, and its input ports can be expanded according to the needs of application scenarios. However, the output power of the SP-MIHR circuit is load dependent and the maximum output power can only be achieved at the optimum load value, but this problem can be well solved using the MPPT technique.

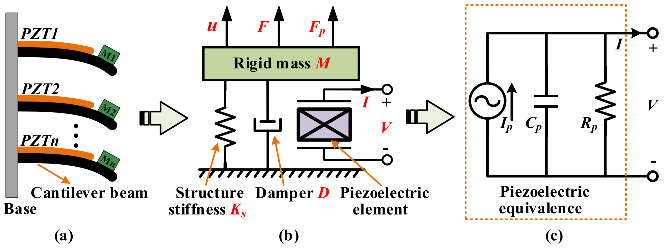

Fig. 1. Mechanical model and equivalent circuit. (a) Multiple PZTs harvester. (b) Equivalent electromechanical model of PZT. (c) Simplified circuit model under resonance conditions.

This article is organized as follows. The typical multi-input S-SSHI circuit topology and the proposed SP-MIHR system structure are introduced in Section II. In Section III, the circuit implementation is discussed in detail. Section IV reports the experimental results, and Section V concludes the article.

II. PROPOSED SP-MIHR TOPOLOGY

A. Equivalent Electrical Model of PZT

A typical piezoelectric cantilever structure for vibration EH is shown in Fig. 1(a), which can be characterized by a mechanical spring system coupled to an electrical domain model. The electrical domain model can be described as a mass-spring-damping system with only one degree of freedom, as depicted in Fig. 1(b). When the vibration acts on the PZT as an external force (F), its tail produces a tip displacement (u), which converts mechanical energy into electric energy. In Fig. 1(b), K_S, M, and D, respectively, denote the structure stiffness, the rigid mass, and the damper, while F_P represents the reaction to the mechanical structure caused by the inverse piezoelectric effect of the piezoelectric element. According to the law of conservation of energy, the input energy of the system can be converted into kinetic energy, elastic energy, mechanical loss, and converted energy. Among them, the converted energy is the sum of the electrostatic energy stored on the capacitor C_P and the energy transferred to the interface circuit [27]

$$\int Fudt = \frac{1}{2}M\dot{u}^2+\frac{1}{2}K_E u^2 + \int D\dot{u}^2 dt + \int \alpha V\dot{u}dt \qquad (1)$$

$$\int \alpha V\dot{u}dt = \frac{1}{2}C_P V^2 + \int VIdt \qquad (2)$$

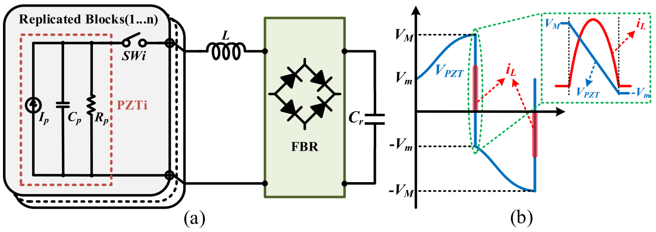

Fig. 2. Typical multi-input S-SSHI circuit topology and waveforms. (a) Multi-input S-SSHI circuit topology. (b) Waveform of voltage (V_{PZT}) and current (i_L).

where α and K_E are the piezoelectric coefficient and stiffness of the piezoelectric element at short-circuit conditions, respectively. When the PZT operates near its resonant frequency, the output current reaches the maximum, and the PZT model can be equivalent to a circuit model with a parallel combination of current source I_P, parasitic capacitor C_P, and resistor R_P, as shown in Fig. 1(c). In the later analysis, the PZT is assumed to be based on the simplified circuit model.

B. Typical Multi-Input S-SSHI Circuit

As shown in Fig. 2(a), the typical multi-input S-SSHI circuit consists of replicated blocks, an inductor, an FBR, and a storage capacitor C_r, where each replicated block contains a PZT and a switch SW. For each PZT, before the vibration displacement reaches the extreme value, the corresponding SW is turned OFF, the whole circuit is at the open state, and the equivalent current source I_P charges the parasitic capacitor C_P. When the voltage of C_P reaches the maximum, the SW is turned ON, and the parasitic capacitor C_P forms a CLC resonance with the inductor L and the storage capacitor C_r. After half a resonance cycle, the SW is turned OFF, the energy extraction process ends, and the voltage on the PZT flips from V_M to -V_m, as shown in Fig. 2(b). In a period, the maximum output power of the circuit can be expressed as

$$P_{\mathrm{S-SSHI,max}} = \frac{f\alpha^2 u_M^2}{C_P}\frac{1+\gamma_S}{1-\gamma_S} \tag{3}$$

where α and u_M are the pressure coefficient and displacement amplitude of the PZT respectively, while γ_S is the voltage flip factor of the S-SSHI circuit. As can be seen from Fig. 2(b), the inductor currents of a typical S-SSHI circuit are opposite in the positive and negative half cycles. Therefore, when the phase difference between the two PZTs is π and the inductor needs to be used to transfer energy at the same time, the energy in the inductor will be offset. Moreover, the presence of an FBR in a typical S-SSHI circuit results in a higher start-up voltage of the circuit, which is at least

$$V_{\mathrm{star,S-SSHI}} = V_{\mathrm{SW}} + 2V_D \tag{4}$$

where V_{SW} is the turn-on voltage of the switch and V_D is the threshold voltage of the diode.

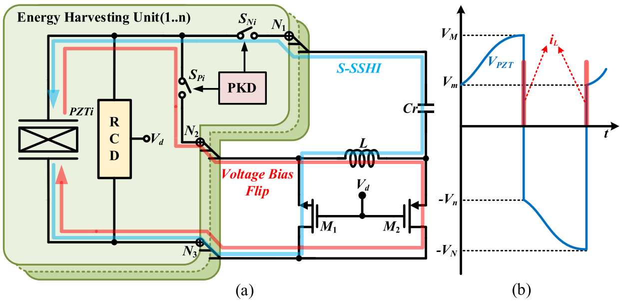

Fig. 3. Proposed SP-MIHR circuit topology and waveforms. (a) SP-MIHR topology. (b) Waveforms of voltage (V_{PZT}) and current (i_L).

C. Proposed SP-MIHR Topology

The proposed SP-MIHR circuit topology is shown in Fig. 3(a). Each EH unit consists of a PZT, two switches, a PKD, and an RCD. These EH units are interconnected via ports N_1, N_2, and N_3, which also connect them to the back-end circuit, so that each EH unit shares a single inductor and MOS switches M_1 and M_2. Due to the uniform direction of the current flowing through the inductor in each EH unit, multiple PZTs can harvest energy together not only by the inductor in TDM but also by the inductor in synchronous extraction.

In the positive half cycle, when the V_{PZT} reaches the peak value, the PKD controls the switch S_{Pi} to turn ON, and the RCD outputs a negative pulse signal, causing the MOSFET M_2 to turn ON. The parasitic capacitor C_P and the inductor L form an LC resonance, and the circuit operates in the voltage bias flip mode. After 1/2 resonance cycle, the voltage of capacitor C_P is reversed. In the negative half cycle, when V_{PZT} reaches the peak value, the PKD controls the switch S_{Ni} to turn ON, and the RCD outputs a positive pulse signal to turn ON the MOSFET M_1. The capacitor C_P forms a CLC resonance with the inductor and capacitor C_r, and the circuit operates in the S-SSHI mode. As shown in Fig. 3(b), the current source I_P charges the capacitor C_P before the switch is turned ON, and the variation amount of the open-circuit voltage of the PZT in a half cycle can be expressed as

$$\triangle\ V = V_M - V_m = V_N - V_n = \frac{1}{C_P}\int_0^{T/2} I_P dt = \frac{2\alpha u_M}{C_P}. \tag{5}$$

The variations of V_{PZT} in the voltage bias flip mode and S-SSHI mode can be, respectively, described as follows:

$$V_n = \gamma_P V_M \tag{6}$$

$$V_m + V_{\mathrm{DC}} = \gamma_S (V_N - V_{\mathrm{DC}}) \tag{7}$$

where γ_P and γ_S are the voltage inversion factors in voltage bias flip mode and S-SSHI mode, respectively, and V_{DC} is the output voltage of the SP-MIHR circuit. According to the working principle of the SP-MIHR circuit, the circuit only transfers energy to the load in S-SSHI mode during each cycle. The transferred energy can be expressed as follows:

$$E_{\mathrm{SP-MIHR}} = V_{\mathrm{DC}} \int_0^{T/2} I dt = V_{\mathrm{DC}} C_P (V_m + V_N) = \frac{2\pi V_{\mathrm{DC}}^2}{\omega R_L}. \tag{8}$$

The following can be derived from the above equations:

$$V_{\mathrm{DC}} = \frac{2\alpha u_M}{C_P} \cdot \frac{\gamma_S(1+\gamma_S)(1+\gamma_P)}{\frac{2\pi\gamma_S(1-\gamma_P\gamma_S)}{\omega R_L C_P} - (1+\gamma_S)(1-\gamma_P\gamma_S) - (1+\gamma_S)^2}. \tag{9}$$

Therefore, the average output power of the SP-MIHR circuit in one cycle can be expressed as:

$$P = V_{\mathrm{DC}}^2 / R_L. \tag{10}$$

When the vibration amplitude of the PZT remains constant, the average output power is maximized at optimum load conditions, which are given as

$$P_{\mathrm{SP-MIHR,max}} = \frac{f\alpha^2 u_M^2}{C_P} \frac{(1+\gamma_S)(1+\gamma_P)}{1-\gamma_P\gamma_S} \tag{11}$$

$$R_{L,\mathrm{opt}} = \frac{1-\gamma_P\gamma_S}{f C_P (1+\gamma_S)(1+\gamma_P)}. \tag{12}$$

According to (11), the maximum output power of the SP-MIHR circuit is closely related to the voltage inversion factor for each operating mode. Typically, $\gamma_P, \gamma_S \in [0,1]$, and $\gamma_P > \gamma_S$. By comparing the maximum output power between SP-MIHR and S-SSHI circuits, the following can be inferred:

$$\frac{P_{\mathrm{SP-MIHR,max}}}{P_{\mathrm{S-SSHI,max}}} = 1 + \frac{\gamma_P - \gamma_S}{1 - \gamma_S\gamma_P} > 1. \tag{13}$$

According to (13), theoretically, the maximum output power of the proposed SP-MIHR circuit is theoretically higher than that of the S-SSHI circuit, indicating the superiority of the former in terms of output power. Additionally, due to the absence of an FBR in the SP-MIHR circuit, the start-up voltage is lower, which can be expressed as

$$V_{\mathrm{star,SP-MIHR}} = V_{\mathrm{SW}} + V_{\mathrm{OD}}. \tag{14}$$

Among them, V_{OD} represents the overdrive voltage of the MOSFET, which is approximately 200 mV, much smaller than the threshold voltage V_D of the diode. From (4) and (14), the start-up voltage of the proposed SP-MIHR circuit is lower than that of the S-SSHI circuit.

III. IMPLEMENTATION OF THE SP-MIHR

To clearly illustrate the working principle of the proposed SP-MIHR circuit clearly, two specific implementations of the SP-MIHR circuit are used to introduce the EH for single PZT and multiple PZTs, respectively.

A. EH for Single PZT

The specific implementation circuit of the proposed topology with a single PZT is shown in Fig. 4. Here, capacitor C_1 and transistors Q_1, Q_2 constitute the PKD to control the switch formed by transistors Q_3, Q_4. The capacitor C_d and resistor R_d form the RCD, which can generate pulse signals to control the on-off function of MOSFETs M_1 and M_2. Transistors Q_3 and Q_4 correspond to switches S_{Ni} and S_{Pi} in Fig. 3, while diodes D_1 and D_2 are used to counteract the reverse parasitic diodes within M_1 and $M_{2,}$ respectively.

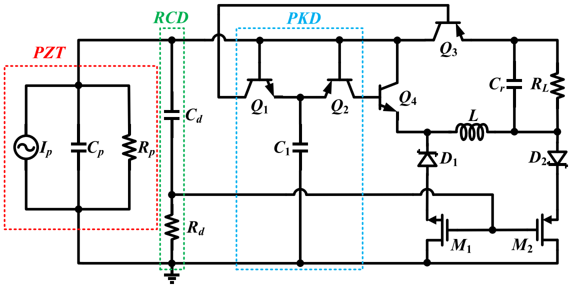

Fig. 4. Proposed SP-MIHR circuit with single PZT.

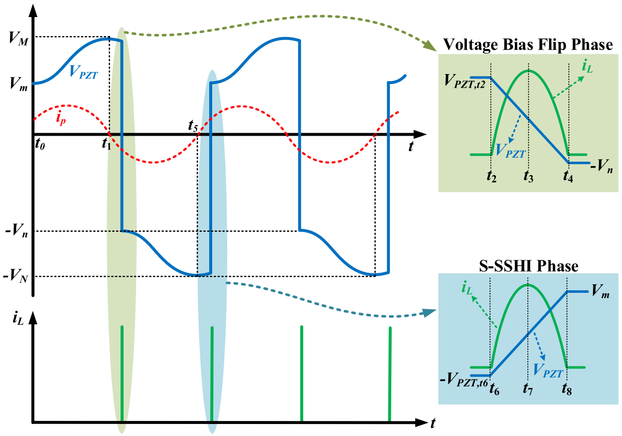

Fig. 5. Waveforms of the SP-MIHR circuit.

The SP-MIHR circuit operates in two different modes. During the positive half-cycle of the PZT vibration, the circuit operates in the voltage bias flip mode, while during the negative half-cycle of the PZT vibration, the circuit works in the S-SSHI mode. The voltage and current waveforms of these modes are depicted in Fig. 5. In order to explain the working principle of the circuit in detail, the six working phases in both modes are analyzed in combination with Fig. 6.

1) Positive Natural Charging Phase (t_0–t_1): As shown in Fig. 6(a), during the forward vibration of the PZT, the current source I_P charges the capacitor C_P, simultaneously charging the PKD capacitor C_1 through the base-emitter junction of transistor Q_1. When the current source I_P becomes zero, the open-circuit voltage of the PZT reaches the maximum value V_M, which can be expressed as follows:

$$V_M = V_m + \frac{1}{C_P}\int_{t_0}^{t_1} I_P dt = V_m + \frac{2\alpha u_M}{C_P}. \tag{15}$$

At this point, the voltage of capacitor C_1 can be expressed as follows:

$$V_{C1} = V_M - V_{\mathrm{be}} \tag{16}$$

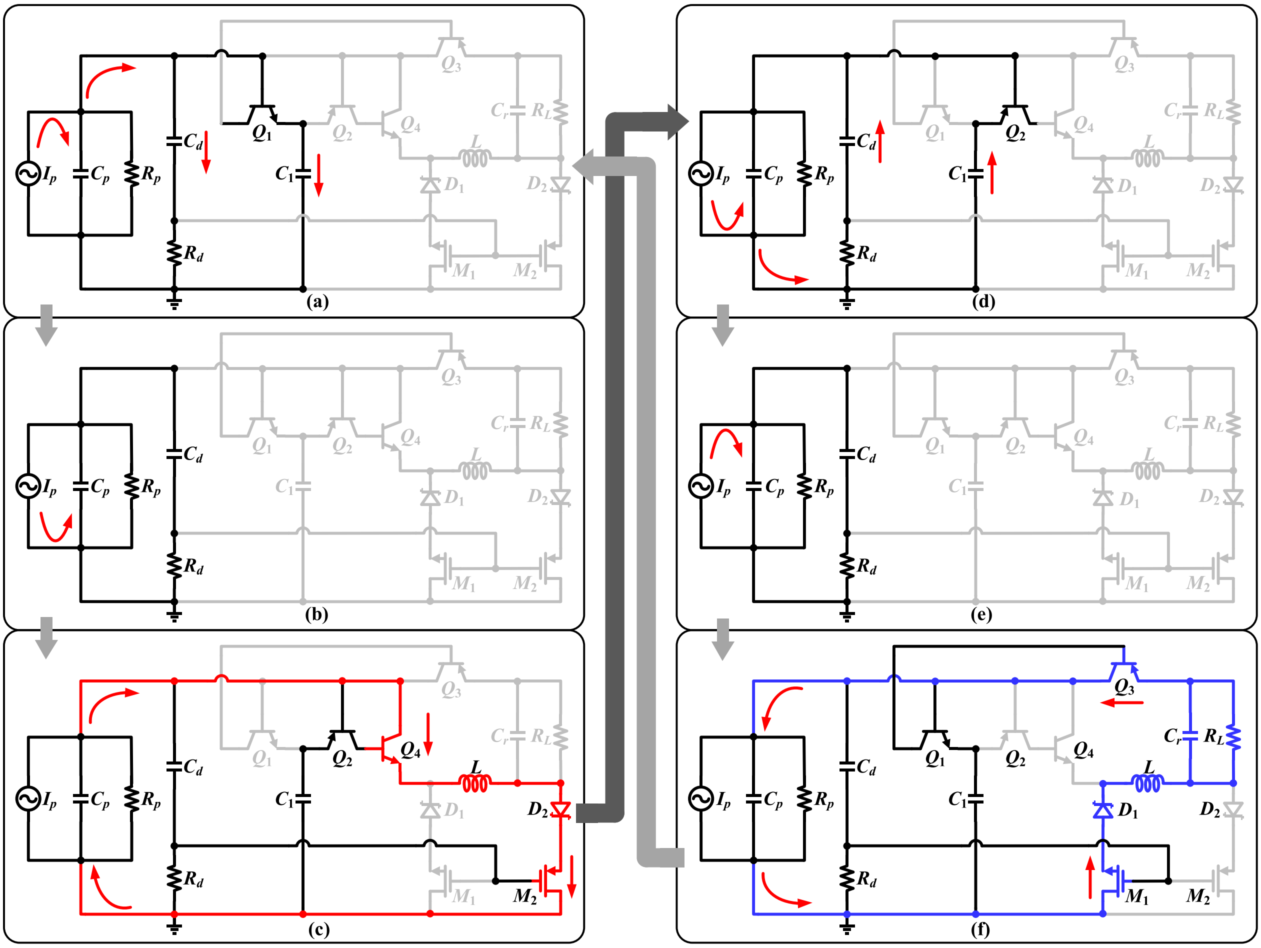

Fig. 6. Six operation phases of the proposed SP-MIHR circuit. (a) Positive natural charging phase. (b) First current reversion phase. (c) Voltage bias flip phase. (d) Negative natural charging phase. (e) Second current reversion phase. (f) S-SSHI phase.

where V_{be} represents the base-emitter junction conduction voltage of the transistor.

2) First Current Reversion Phase (t_1–t_2): As illustrated in Fig. 6(b), during the reverse vibration of the PZT, the current source I_P inversely charges the capacitor C_P, causing the voltage of C_P to decrease. Owing to the presence of the base-emitter junction of transistor Q_2, the voltage of C_1 remains constant. The transistor Q_2 becomes conductive when the voltage difference between C_1 and C_P is greater than the conduction voltage of the transistor base-emitter junction, thus driving the conduction of transistor Q_4, and then the circuit works in the third phase. At this point, the open-circuit voltage of the PZT is given by

$$V_{\mathrm{PZT},t2} = V_{C1} - V_{\mathrm{be}} = V_M - 2V_{\mathrm{be}}. \qquad (17)$$

This also indicates a phase difference between the moment of switch conduction and the moment when V_{PZT} reaches its peak, which can be expressed as follows:

$$\theta = \cos^{-1}\left[(V_M - 2V_{\mathrm{be}})/V_M\right]. \qquad (18)$$

The energy loss attributable to the phase difference can be represented as

$$\triangle E_\theta = \frac{1}{2}C_P\left(V_M^2 - V_{\mathrm{PZT},t2}^2\right) = \frac{1}{2}C_P V_M \sin^2\theta. \qquad (19)$$

From (19), it is evident that an increase in the phase difference corresponds to an increase in energy loss, resulting in a reduced efficiency of the EH. The relationship between the efficiency of the EH and the phase difference can be expressed as follows:

$$\eta = \frac{\frac{1}{2}C_p V_M^2 - \triangle E_\theta}{\frac{1}{2}C_p V_M^2} = \cos^2\theta. \qquad (20)$$

3) Voltage Bias Flip Phase (t_2–t_4): As shown in Fig. 6(c), when the transistor Q_4 is turned ON, the voltage of the C_P begins to reverse, leading to the RCD output of a negative pulse signal that triggers the conduction of MOSFET M_2. The capacitor C_P and inductor L then form an LC resonant circuit. After half a resonance period, the voltage of the capacitor C_P is reversed. From t_2 to t_4, the relationship between $V_{\mathrm{PZT},t2}$ and V_n can be expressed as follows:

$$V_n + V_{\mathrm{ec}} + V_{\mathrm{DS}} + V_D = \gamma_P(V_{\mathrm{PZT},t2} - V_{\mathrm{ec}} - V_{\mathrm{DS}} - V_D) \qquad (21)$$

where V_{ec} is the emitter-collector voltage of the transistor Q_4, V_{DS} is the drain-source voltage of the MOSFET M_2, and V_D is the threshold voltage of the diode.

4) Negative Natural Charging Phase (t_4–t_5): As shown in Fig. 6(d), this process is similar to the positive natural charging

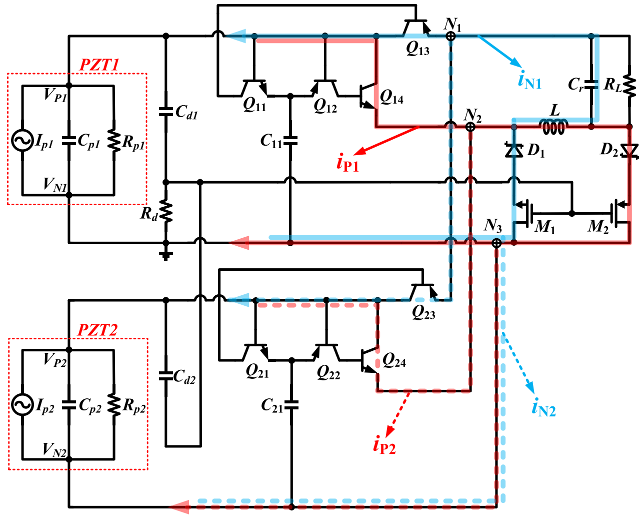

Fig. 7. Proposed SP-MIHR circuit with two PZTs.

phase. The current source I_P charges the capacitor C_P, while I_P also charges the capacitor C_1 through the transistor Q_2. When I_P reaches zero, the voltage of C_P reaches the negative peak value, $-V_N$.

5) Second Current Reversion Phase (t_5–t_6): As shown in Fig. 6(e), this process is similar to the first current reversion phase. The transistor Q_1 becomes conductive when the voltage difference between C_1 and C_P is greater than the transistor base-emitter junction conduction voltage, thus driving the conduction of transistor Q_3, and then the circuit works in the next phase.

6) S-SSHI Phase (t_6–t_8): As shown in Fig. 6(f), when the transistor Q_3 is turned ON, the voltage of the C_P begins to reverse, resulting in the RCD output of a positive pulse signal that triggers the conduction of MOSFET M_1. The capacitor C_P forms an *LC* resonant loop with MOSFET M_1, inductor L, capacitor C_r, and transistor Q_3. After 1/2 resonance period, part of the energy stored in capacitor C_P is transferred to C_r, while another part returns to C_P, resulting in voltage inversion. At this phase, the change in voltage of C_P and the energy stored in C_r can be represented as follows:

$$V_m + V_{\mathrm{DC}} + V_{\mathrm{ec}} + V_{\mathrm{DS}} + V_D = \gamma_S(V_{\mathrm{PZT},t6} - V_{\mathrm{DC}} - V_{\mathrm{ec}} - V_{\mathrm{DS}} - V_D) \tag{22}$$

$$E_{\mathrm{Cr}} = V_{\mathrm{DC}} \cdot \int_{t6}^{t_8} i_L(t)dt = V_{\mathrm{DC}} C_P(V_m + V_{\mathrm{PZT},t6}) \tag{23}$$

where V_{DC} is the voltage of C_r, V_{ec} is the emitter-collector voltage of the transistor Q_3, and V_{DS} is the drain-source voltage of the MOSFET M_1.

B. EH for Multiple PZTs

In order to facilitate the discussion, a dual PZTs circuit is used as an example to analyze the operating principle of the multiple PZTs EH circuit, as shown in Fig. 7. When both PZTs harvest energy simultaneously, the current through the inductor L flows in the same direction, effectively addressing the issue of charge cancellation encountered in traditional TDM circuits when both PZTs employ the inductor simultaneously. Furthermore, the inductor L, diodes D_1 and D_2, and MOSFETS M_1 and M_2, as well as the resistor R_d within the RCD structure, are all shared in the SP-HIMR circuit. As the number of PZTs increases, this approach not only saves components, but also significantly reduces the size of the circuit, thereby reducing the power dissipation.

TABLE I
COMPONENT MODELS AND PARAMETERS

Component	Models or Parameters
C_{11}, C_{21}	2nF
C_{d1}, C_{d2}	2.2nF
L	1.8mH
I_{p1}, I_{p2}	85μA/34Hz
R_d, R_{p1}/R_{p2}	510kΩ, 2MΩ
C_r, C_{p1}/C_{p2}	220μF, 132nF
NPN (Q_{11}, Q_{14}, Q_{21}, Q_{24})	2N3904
PNP (Q_{12}, Q_{13}, Q_{22}, Q_{23})	2N3906
NOMS (M_1)	AO6408
POMS (M_2)	AO6407
Schottky Diode (D_1, D_2)	1N5819

In practical applications, the vibration amplitude and frequency of PZTs fluctuate in response to environmental changes, resulting in arbitrary phase differences between multiple PZTs. For a circuit containing two PZTs, the phase difference during inductor operation can be categorized into four different situations. For a comprehensive understanding of the EH of multiple PZTs, the four cases are simulated using LT-Spice software, and the circuit component models and parameters used in the simulation are shown in Table I. The details are as follows.

1) *Complete synchronization ($\varphi = 0$):* When the phase difference φ between PZT1 and PZT2 is equal to 0, it indicates that the open-circuit voltages V_{PZT} of both PZTs reach their peak simultaneously, requiring the simultaneous use of an inductor for energy transfer. In this case, transistors Q_{14} and Q_{24} are concurrently conductive, and the RCD outputs a negative pulse signal to control the MOSFET M_2 to be turned ON. Then C_{P1} and C_{P2} are connected in parallel, forming an *LC* resonant loop with the inductor L. As a result, the voltage and current waveforms of both PZTs overlap, and the inductor current *I(L)* is the sum of the current *I*(C_{P1}) of the C_{P1} and the current *I*(C_{P2}) of the C_{P2}, as shown in Fig. 8(a).
2) *Complete asynchronization ($\pi < \varphi < 2\pi$):* Considering that the operating time of the inductor is extremely short compared to the vibration cycle, and that the vibration frequency of the PZTs is influenced by environmental factors, the two PZTs predominantly work in a complete asynchronous state. In this case, the two PZT units operate independently of each other without mutual interference, and their use of the inductor is separate, eliminating conflicts in the use of the inductor. The operating principle of the circuit is similar to that of the traditional TDM method, with the corresponding voltage and current waveforms illustrated in Fig. 8(b).

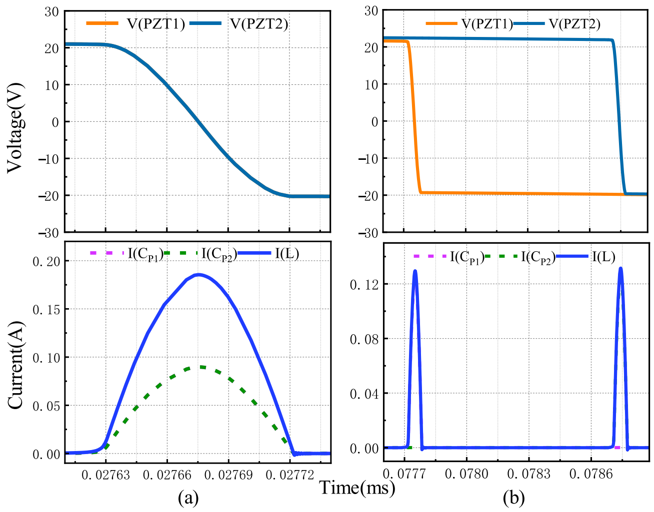

Fig. 8. Voltage and current waveforms. (a) Complete synchronization. (b) Complete asynchronization.

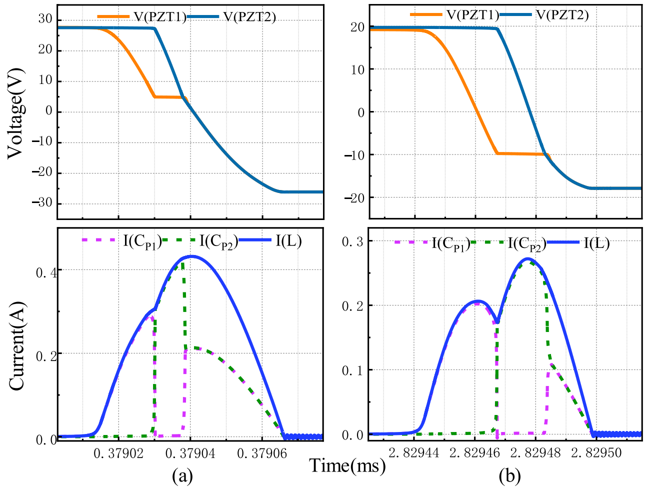

Fig. 9. Voltage and current waveforms. (a) Continuous inductor charging. (b) Continuous inductor discharging.

3) *Continuous inductor charging* $(0 < \varphi < \pi/2)$: In this case, the phase difference between the two PZTs is very small, and as shown in Fig. 9(a), V_{PZT1} reaches its peak before V_{PZT2}. At this time, the PKD control transistor Q_{13} corresponding to the PZT1 unit is turned ON, while the RCD outputs a positive pulse signal to control the conduction of the MOSFET M_1. Then C_{P1}, the inductor L, and C_r form an LC resonance. Then C_{P1} begins to charge the inductor L, resulting in a decrease in V_{PZT1} and an increase in inductor current *I(L)*. During this period, the V_{PZT2} reaches the peak, the transistor Q_{23} and the MOSFET M_1 are turned ON, allowing C_{P2} to also form an LC resonance with the inductor L and C_r. At this time, since $V_{\text{PZT2}} > V_{\text{PZT1}}$, transistor Q_{13} is temporarily OFF, clamping V_{PZT1}. As V_{PZT1} decreases to equalize with V_{PZT2}, transistor Q_{13} becomes conductive again, allowing both C_{P1} and C_{P2} to simultaneously charge the inductor L until the inductor current I_L peaks. The circuit then enters an inductor discharge phase in which the inductor current *I(L)* is equal to the sum of I(C_{P1}) and I(C_{P2}).

4) *Continuous inductor discharging* $(\pi/2 < \varphi < \pi)$: As shown in Fig. 9(b), in this case, the V_{PZT1} reaches the peak before the V_{PZT2}, but unlike the previous stage, when V_{PZT2} reaches its peak, PZT1 is in the inductor discharge state. At this point, $V_{\text{PZT2}} > V_{\text{PZT1}}$, leading to the clamping of V_{PZT1} and interruption of the inductor discharge, causing *I(C_{P1})* to instantaneously drop to 0. Subsequently, the charge within C_{P2} begins to be extracted, resulting in V_{PZT2} decreasing and *I(C_{P2})* increasing. When V_{PZT1} decreases to equalize with V_{PZT2}, both PZTs are simultaneously in inductor discharge, with the inductor current being the sum of the currents from each PZT.

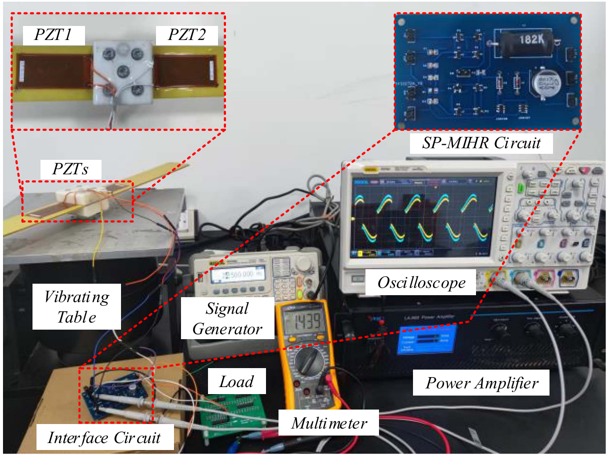

Fig. 10. Experimental setup.

Through the analysis of the above four cases, it is evident that the proposed circuit solves the queuing problem of using an inductor in the traditional TDM circuit, which also shows that the proposed SP-MIHR circuit can extract energy from multiple PZTs with arbitrary phase difference $(0{-}2\pi)$.

IV. EXPERIMENTAL WORK

A. *Experimental Setup*

To physically verify the effectiveness of the proposed SP-MIHR circuit, the experimental test platform is constructed as depicted in Fig. 10. The experimental setup mainly consists of a vibration table (VT-500), a signal generator (DG1022U), an oscilloscope (DSOX4024A), a power amplifier (LA-800), two PZTs (M-5628-P2/C_{p} = 132 nF), a multimeter, a load board, and the SP-MIHR interface circuit. The other components of the circuit are the same as in the simulation (see Table I).

By adjusting the signal generator, a sinusoidal signal with modulated frequency and amplitude can be generated. The sinusoidal signal, after being amplified by the power amplifier, can be used to control the vibration table, causing the PZT to vibrate. Two identical PZTs are mounted on opposite sides of a cantilever beam to maintain symmetry. The resonant frequency can be adjusted by changing the position of the cantilever. In

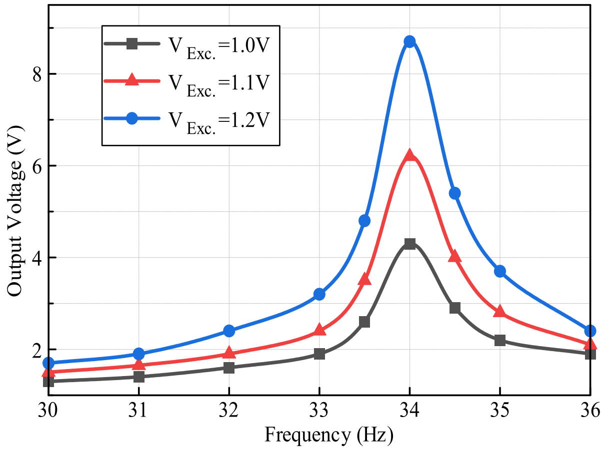

Fig. 11. Waveforms of the output voltage versus frequency with different excitation amplitude.

TABLE II
OPEN CIRCUIT VOLTAGE OF PZT WITH DIFFERENT ACCELERATION

Acceleration (m/s^2)	1.25	1.38	2.16	2.79	3.37
Open Circuit Voltage (V)	1	1.4	3	4	5

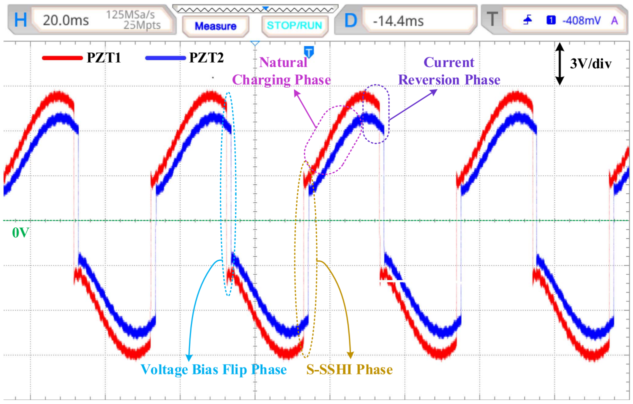

Fig. 12. Measured PZTs voltage waveform of the SP-MIHR circuit.

the experiment, the oscilloscope can be used to observe the waveform of the circuit, the maximum output power of the circuit can be measured by changing the load size of the access circuit, and the multimeter can be used to measure the load voltage.

To obtain the frequency response of the piezoelectric devices used, we measured the output voltage of the PZT versus frequency at different excitation amplitudes, as shown in Fig. 11. It can be seen that the output voltage of the PZT reaches its maximum value only at the resonance frequency, and the resonance frequency of the PZT is 34 Hz. The acceleration applied to the piezoelectric energy harvester at different no-load voltages was measured using a vibrometer (VICTOR 63B), as shown in Table II. The SP-MIHR circuit starts to harvest energy when the acceleration is greater than 1.38 m/s^2.

B. Analysis of Waveforms

Fig. 12 shows the voltage V_{PZT} waveform of the SP-MIHR circuit measured by the oscilloscope, revealing that the two PZTs are operating in the complete asynchronization state. During the positive half cycle, each PZT reaches the voltage peak after the natural charging phase and then, after a short delay, the voltage begins to flip. There is a phase difference between the maximum voltage and the voltage just before flipping, estimated to be about $2V_{\mathrm{be}}$ (1.2 V), which confirms the theoretical analysis formulated in Section III-A. In the negative half cycle, the voltage of each PZT is flipped and extracted near the peak, and the circuit operates in the S-SSHI mode. During this phase, energy is transferred from the PZTs to the energy storage capacitor as shown in (23). The above analysis demonstrates that the proposed circuit can alternately perform voltage bias flip mode and S-SSHI mode in one cycle, which is consistent with the theoretical analysis.

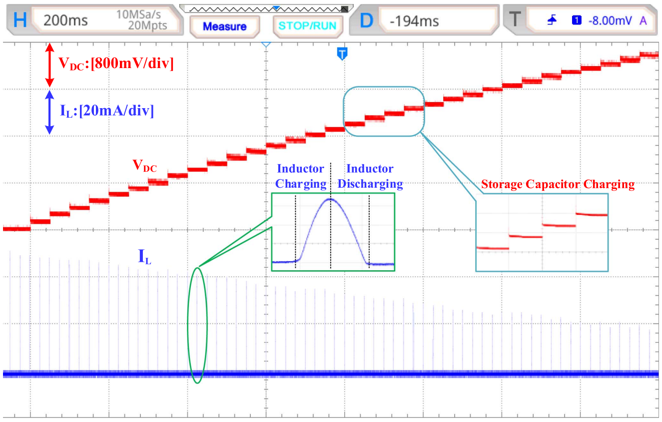

Fig. 13. Waveforms of inductor current and output voltage.

Fig. 13 shows the waveforms of the inductor current and output voltage. It can be seen that the inductor is used twice in a cycle, while the energy storage capacitor is only charged once, due to the fact that the PZT transfers energy to the storage capacitor only in the S-SSHI mode. Moreover, it can be observed that the direction of the inductor current remains constant throughout the cycle and the output voltage increases stepwise during the charging process. However, as the output voltage increases, the inductor current gradually decreases, because the inductor current is limited by the increase of output voltage. The relationship between output voltage and inductor current can be expressed as follows:

$$I_{L,\max} = \sqrt{C_p/L} \cdot (V_N - V_{\mathrm{DC}} - V_{\mathrm{ec}} - V_D - V_{\mathrm{DS}}). \quad (24)$$

According to (24), as the output voltage increases to the maximum, the inductor current will decrease to 0, and the circuit will not be able to harvest energy from the PZT, which means that the proposed circuit can only maintain high efficiency at the optimal output voltage.

In order to verify that the SP-MIHR circuit can extract energy from multiple PZTs with different phase differences, we install two identical PZTs on the symmetrical position of the same cantilever beam and then tune the frequency of the vibration table to change the phase difference between the two PZTs. The voltage and inductor current waveforms of the two PZTs at different phase differences are tested, as depicted in Fig. 14. It can be observed that the experimentally measured voltage and

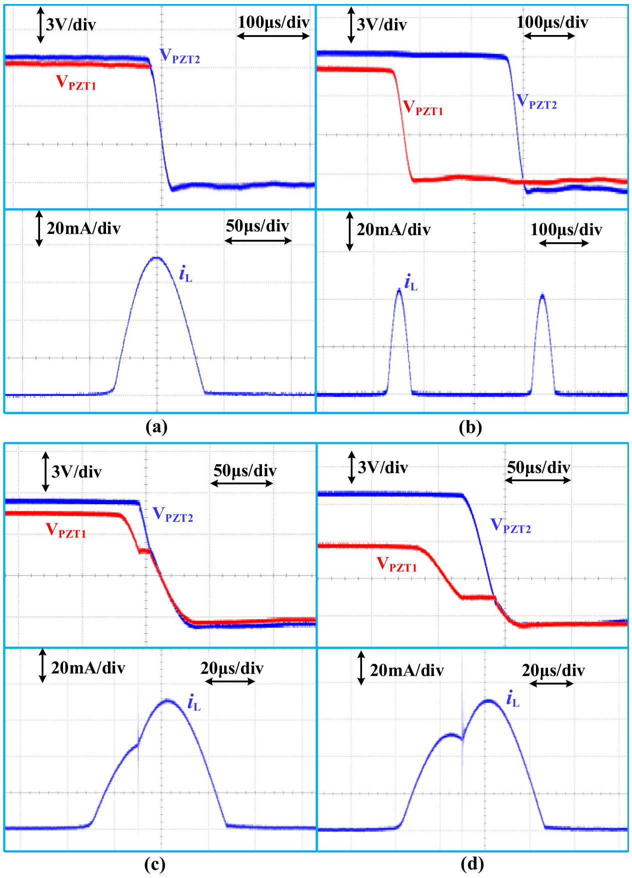

Fig. 14. Voltage and current waveforms in four cases. (a) Complete synchronization. (b) Complete asynchronization. (c) Continuous inductor charging. (d) Continuous inductor discharging.

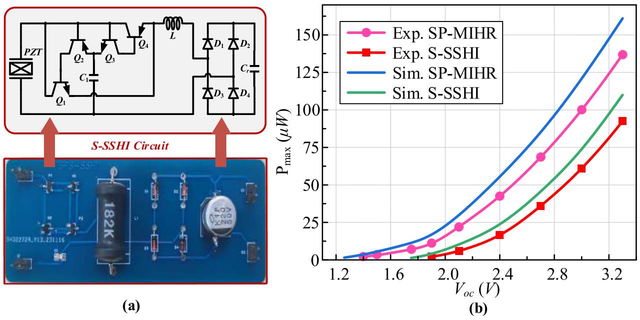

Fig. 15. Circuit and waveforms. (a) Traditional S-SSHI circuit. (b) Maximum output power waveforms at different open-circuit voltages of the PZT.

inductor current waveforms are consistent with the simulation, which shows that the proposed circuit can extract energy from multiple PZTs with arbitrary phase difference ($0-2\pi$).

C. Experimental Results

In order to ascertain the start-up voltage of the proposed circuit, we measured the maximum output power of the SP-MIHR circuit at different open-circuit voltages of the PZT and compared it with the simulation results, as shown in Fig. 15(b). For comparison purposes, a prototype of the S-SSHI circuit was also fabricated using the same discrete components, with a detailed circuit implementation presented in Fig. 15(a). It can be observed that the start-up voltage of the SP-MIHR circuit is 1.4 V, which is significantly lower than the 1.9 V of the S-SSHI circuit. This is because there is no FBR structure in the SP-MIHR circuit, and the overdrive voltage of the MOSFET in the SP-MIHR circuit is less than the threshold voltage of the FBR diode in the S-SSHI circuit. As the open-circuit voltage of the PZT increases, the output power of both the SP-MIHR and S-SSHI circuits also increases, and the maximum output power of the proposed circuit is always higher than that of the S-SSHI circuit, which is consistent with the theoretical analysis in (13). The measured results deviate from the simulation results by approximately 12%. This is because the simulations use the simplified equivalent circuit, which does not take into account the mechanical effects induced by power extraction, leading to an overestimation of its performance.

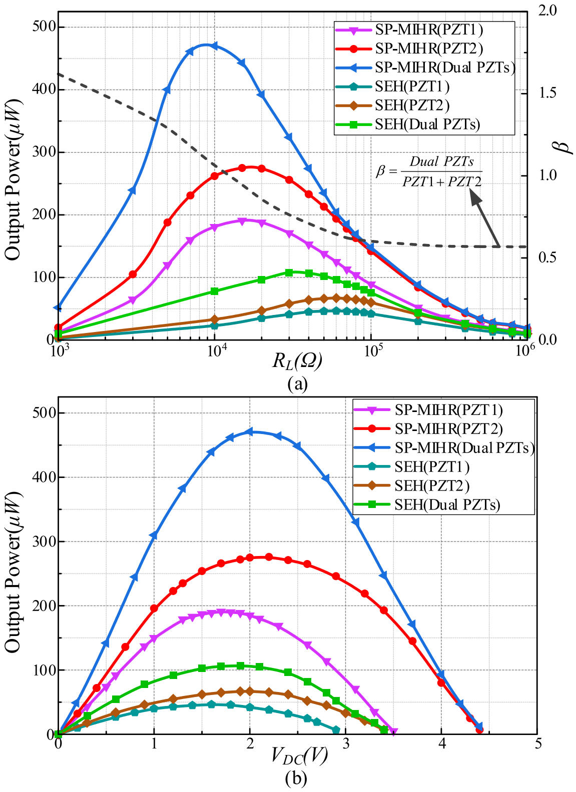

Fig. 16. Output power characteristics of the SP-MIHR circuit. (a) Output power versus load R_L. (b) Output power versus the output voltage V_{DC}.

Compared with the S-SSHI circuit, the start-up voltage of the SP-MIHR circuit is 0.5 V lower than that of the S-SSHI circuit, and the maximum output power of the SP-MIHR circuit is 1.47 times that of the S-SSHI circuit, which fully illustrates the high efficiency of the proposed circuit.

To measure the EH efficiency of the proposed circuit for multiple PZTs, an experiment was carried out where two PZTs ($V_{\mathrm{oc1}} = 4$ V, $V_{\mathrm{oc2}} = 4.5$ V) were connected to the circuit, and compared with the SEH circuit under identical conditions, as depicted in Fig. 16. In Fig. 16(a), a dual ordinate axis is used, where the left axis represents the output power, which represents

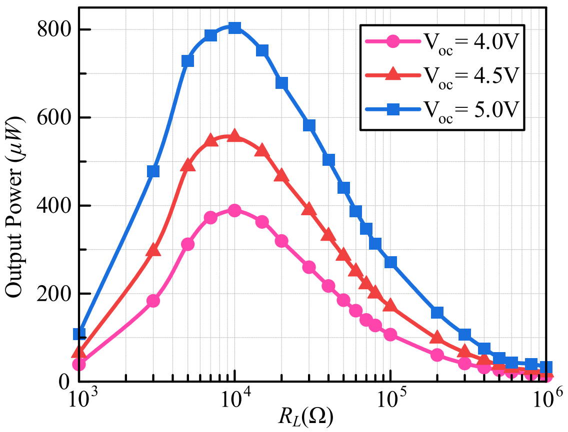

Fig. 17. Waveforms of output power versus load R_L with different V_{oc}.

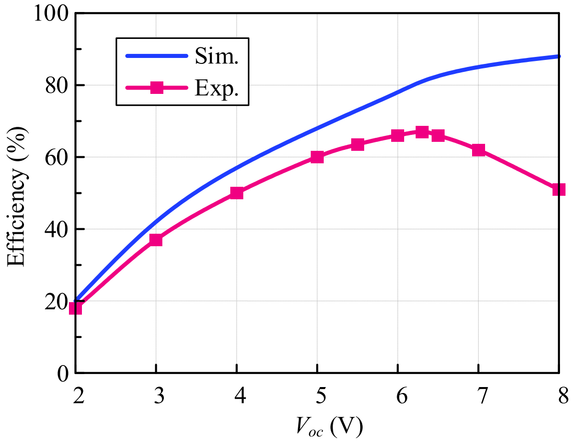

Fig. 18. Energy conversion efficiency with different V_{oc} ($f = 34$ Hz).

the performance of the circuit at different loads, while the right axis represents the ratio β of the output power of two PZTs operating simultaneously to the sum of the output power of the two PZTs operating separately in the SP-MIHR circuit, which represents the multi-input characteristic of the SP-MIHR circuit that varies with load.

As shown in Fig. 16(a), the output power of the SP-MIHR circuit is influenced by the load, reaching its maximum only at the optimal load resistance. For a single PZT, the optimal load resistance is approximately 15 kΩ, whereas for dual PZTs, the optimal load resistance is about 10 kΩ. This is attributable to the fact that, for the EH of dual PZTs, the output voltage V_{DC} rises more quickly for the same load resistance, thereby reducing the optimal load value. The dotted line in the figure illustrates that for loads of less than 11 kΩ, the output power of the dual PZTs exceeds the sum of the output powers of PZT1 and PZT2 individually, which also proves that the SP-MIHR circuit can effectively extract energy from multiple PZTs. The maximum output power of the SP-MIHR circuit with two PZT inputs is 466 μW, while the maximum output power of the SEH circuit is 113 μW. Therefore, compared with the SEH circuit, the maximum output power of the SP-MIHR circuit is 4.12 times higher than that of the SEH circuit.

As depicted in Fig. 16(b), the optimal output voltage corresponds to the maximum output power. Due to the difference in open-circuit voltages between PZT1 and PZT2, their respective optimal output voltages are also different, with the optimal output voltages of PZT1 and PZT2 being about 1.8 and 2.2 V, respectively. For the EH of the dual PZTs, the optimal output voltage is between 1.8 and 2.2 V. This is because when the output voltage V_{DC} exceeds the optimal output voltage (1.8 V) of PZT1, the output power of PZT1 decreases as V_{DC} increases, while the output power of PZT2 increases as V_{DC} increases, resulting in almost no change in the combined output power of PZT1 and PZT2. The output voltage range of the SP-MIHR circuit with dual PZT inputs is 0–4.4 V, while the output voltage range of the SEH circuit is 0–3.4 V. Therefore, compared with the SEH circuit, the output voltage range of the SP-MIHR circuit is 1.3 times that of the SEH circuit.

TABLE III
HARVESTED POWER AND POWER LOSS

Input Voltage (V)	Power Loss (μW)		Harvested Power (μW)
	$P_{L,1}$	$P_{L,2}$	
V_{oc1}=V_{oc2}=4.0	152	224	384
V_{oc1}=V_{oc2}=4.5	176	297	556
V_{oc1}=V_{oc2}=5.0	204	332	804

Fig. 17 shows the output power versus the equivalent load resistance of the SP-MIHR circuit with dual PZT inputs at different input voltages (V_{OC}). It can be seen that the power curves of the SP-MIHR circuits at different input voltages are similar in trend and shape, and the output power increases as the input voltage increases. In addition, the output power of the SP-MIHR circuit is greatly affected by the load, and the output power reaches its maximum value when the load resistor is 10 kΩ.

Fig. 18 shows the end-to-end energy conversion efficiency of the SP-MIHR circuit with dual PZT inputs at 34 Hz frequency with different input voltages and the comparison of the experimental results with the simulation results. The energy conversion efficiency of the SP-MIHR circuit is lower at lower input voltages. This is due to the fact that the circuit harvests less energy and loses relatively more of the energy when the input voltage is low, resulting in a lower energy conversion efficiency. As the input voltage increases, the energy conversion efficiency gradually increases, reaching a maximum of 67.3% at an input voltage of 6.3 V and then slowly decreasing. This is because when the input voltage is high, the voltage of the transistors in the circuit reaches saturation, at which point the energy harvested by the circuit remains essentially the same, and therefore the energy conversion efficiency decreases. However, the simulation results are different because the saturation voltage of the transistor is higher in the simulated environment, so the energy conversion efficiency of the simulation results increases as the input voltage increases.

Table III shows the dynamic loss of the SP-MIHR circuit with two PZT inputs. The loss of the whole circuit consists of two parts, $P_{L,1}$ and $P_{L,2}$. One part is the loss generated by the peak detection circuit, called $P_{L,1}$, which is mainly due to the power

TABLE IV
Performance Comparison

Publication	TPEL2021[23]	TPEL2020[25]	TPEL2018[20]	TIE2022[24]	TIE2022[26]	TPEL2021[18]	This Work
PZT	PPA-1014	PPA-1014	PPA-4011	PPA-1001	PPA-1001	PPA-2011	M-5628-P2
Technique	S-SSHI	Buck+SECE	SECE	P-SSHI	ReL-SSHI	S-SSHI+SECE	Bias flip+S-SSHI
Input port	Multi-input	Multi-input	Multi-input	Multi-input	Multi-input	Single input	Multi-input
Self-powered	YES	YES	NO	YES	YES	YES	YES
Frequency	19Hz	20Hz	65Hz	N/R	30Hz	18Hz	34Hz
Inductor	2.3mH	1mH	3.3mH	Dual (10mH+10mH)	47mH	Dual (2mH+10mH)	1.8mH
Required phase	$0 \sim 2\pi$	$0 \sim 2\pi$	$\neq 0, \neq \pi$	$0 \sim 2\pi$	$\neq \pi$	N/A	$0 \sim 2\pi$
Reliability	High	High	Low	High	Medium	Medium	High
Inductor multiplexing mode	TDM+SE	TDM+SE	TDM	TDM+SE	TDM	N/A	TDM+SE
Number of total elements (a PZT)	12	9	N/R	13	N/R	12	13
Number of shared elements	1	3	1	2	1	N/A	5
Power boost to SEH	3.70×	N/R	N/R	4.8×	4.85×	3.41×	4.12×

N/R=Not Reported; N/A=Not Applicable.

dissipation caused by the mismatch between the turn-on time and the time when the PZT voltage reaches its peak. The other part is the power dissipation generated during the LC oscillation, called $P_{L,2}$, which includes the power dissipation due to the parasitic resistance of the inductors and transistors and the power dissipation generated by the circuit during the voltage flipping. It can be seen that the power dissipation is not fixed but varies continuously with the input voltage. In addition, the power loss due to LC oscillation accounts for a relatively large proportion of the power consumed and this loss can be reduced by selecting a high-quality inductor with low parasitic resistance. The power dissipation due to the peak detector switching delay is mainly due to the junction voltage $V_{\rm be}$ of the transistor, and this loss increases as the input voltage increases. The power dissipation due to the switching delay can be reduced by selecting transistors with the lowest possible $V_{\rm be}$ in the circuit design.

The performance comparison between the proposed SP-MIHR circuit and several typical EH circuits is presented in Table IV. Chen et al. [23] and Wang et al. [25] use the S-SSHI and SECE structures, respectively, to harvest energy from PZTs with arbitrary phase differences, but their EH efficiency is inferior to the proposed circuit. In [20], a complex active digital circuit is used to generate precise control signals, but this circuit can only harvest energy from multiple PZTs using the inductor TDM method, which makes this circuit less reliable. In addition, the use of many active devices makes the cost-effectiveness of this circuit high. The P-SSHI circuit in [24] uses a voltage-doubling rectifier structure to reduce the number of switches, but the use of two inductors results in an oversized circuit. In addition, when the circuit is extended to multiple PZT inputs, only the inductors can be shared, which increases the cost of the circuit. In [26], a novel MPPT technique is used to extract energy from PZT arrays, which improves the EH efficiency. However, this circuit cannot handle the PZT phase difference of π, and only the inductor can be shared by PZT arrays. In [18], a hybrid rectifier structure is used to achieve higher EH efficiency and a wider rectified voltage range, but this circuit cannot be expanded. Furthermore, the use of a transformer makes the EH efficiency more sensitive to the coupling coefficient of the inductor and less reliable. In contrast, the circuit proposed in this article employs a simpler structure to extract energy from multiple PZTs with arbitrary phase differences. Moreover, apart from the switches, most of the other components can be shared, significantly reducing the volume of the circuit and the cost cost-effectiveness.

V. Conclusion

In this article, an SP-MIHR with arbitrary phase difference and low start-up voltage is proposed. The proposed circuit effectively improves the output power by using a series-parallel hybrid inductor configuration for the EH. Furthermore, the proposed circuit uses the method of controlling the switch by a combination of the RCD and the PKD to reduce the start-up voltage of the circuit and extract energy from multiple PZTs. An experiment performed on two PZTs demonstrates the SP-MIHR circuit can achieve 4.12× power improvement and 1.3× voltage improvement compared with the multi-input SEH circuit. Compared to the classic S-SSHI circuit, the SP-MIHR circuit delivers 1.47 times more output power and has a start-up voltage that is 0.5 V lower than the S-SSHI circuit. The maximum end-to-end energy conversion efficiency of the proposed circuit is 67.3%. Both the analysis and experiment confirm the SP-MIHR circuit provides an effective solution for multi-PZT EH.

References

[1] J. Wang, Z. Chen, Z. Li, J. Jiang, J. Liang, and X. Zeng, "Piezoelectric energy harvesters: An overview on design strategies and topologies," *IEEE Trans. Circuits Syst. II, Exp. Briefs*, vol. 69, no. 7, pp. 3057–3063, Jul. 2022.

[2] G. Shi, J. Chang, Y. Xia, X. Wang, H. Xia, and Q. Li, "A multisource collaborative energy extraction circuit for vibration, ambient light, and thermal energy with MPPT and single inductor," *IEEE Trans. Ind. Electron.*, vol. 70, no. 6, pp. 5819–5829, Jun. 2023.

[3] X. Wang et al., "Configurable hybrid energy synchronous extraction interface with serial stack resonance for multi-source energy harvesting," *IEEE J. Solid-State Circuits*, vol. 58, no. 2, pp. 451–461, Feb. 2023.

[4] N. Krihely and S. Ben-Yaakov, “Self-contained resonant rectifier for piezoelectric sources under variable mechanical excitation,” *IEEE Trans. Power Electron.*, vol. 26, no. 2, pp. 612–621, Feb. 2011.

[5] J. Liang, Y. Zhao, and K. Zhao, “Synchronized triple bias-flip interface circuit for piezoelectric energy harvesting enhancement,” *IEEE Trans. Power Electron.*, vol. 34, no. 1, pp. 275–286, Jan. 2019.

[6] Z. J. Chew and M. Zhu, “Adaptive self-configurable rectifier for extended operating range of piezoelectric energy harvesting,” *IEEE Trans. Ind. Electron.*, vol. 67, no. 4, pp. 3267–3276, Apr. 2020.

[7] R. C. H. Chang, W. C. Chen, L. Liu, and S. H. Cheng, “An AC–DC rectifier with active and non-overlapping control for piezoelectric vibration energy harvesting,” *IEEE Trans. Circuits Syst. II, Exp. Briefs*, vol. 67, no. 6, pp. 969–973, Jun. 2020.

[8] E. Lefeuvre, A. Badel, A. Benayad, L. Lebrun, C. Richard, and D. Guyomar, “A comparison between several approaches of piezoelectric energy harvesting,” *J. Physique IV (Proc.)*, vol. 128, pp. 177–186, 2005.

[9] E. Lefeuvre, A. Badel, C. Richard, and D. Guyomar, “Piezoelectric energy harvesting device optimization by synchronous electric charge extraction,” *J. Intell. Mater. Syst. Struct.*, vol. 16, no. 10, pp. 865–876, Oct. 2005.

[10] E. Lefeuvre, A. Badel, C. Richard, L. Petit, and D. Guyomar, “A comparison between several vibration-powered piezoelectric generators for standalone systems,” *Sensors Actuators A, Phys.*, vol. 126, no. 2, pp. 405–416, Feb. 2006.

[11] S. J. Yun, S. S. Kwak, J. Lee, Y. C. Im, S.-G. Lee, and Y. S. Kim, “Asymmetric SECE piezoelectric energy harvester under weak excitation,” *IEEE Access*, vol. 8, pp. 99132–99140, 2020.

[12] L. Wu and D. S. Ha, “A self-powered piezoelectric energy harvesting circuit with an optimal flipping time SSHI and maximum power point tracking,” *IEEE Trans. Circuits Syst. II, Exp. Briefs*, vol. 66, no. 10, pp. 1758–1762, Oct. 2019.

[13] S. Li, A. Roy, and B. H. Calhoun, “A piezoelectric energy-harvesting system with parallel-SSHI rectifier and integrated maximum-power-point tracking,” *IEEE Solid-State Circuits Lett.*, vol. 2, no. 12, pp. 301–304, Dec. 2019.

[14] D. A. Sanchez, J. Leicht, F. Hagedorn, E. Jodka, E. Fazel, and Y. Manoli, “A parallel-SSHI rectifier for piezoelectric energy harvesting of periodic and shock excitations,” *IEEE J. Solid-State Circuits*, vol. 51, no. 12, pp. 2867–2879, Dec. 2016.

[15] M. Dini, A. Romani, M. Filippi, and M. Tartagni, “A nanopower synchronous charge extractor IC for low-voltage piezoelectric energy harvesting with residual charge inversion,” *IEEE Trans. Power Electron.*, vol. 31, no. 2, pp. 1263–1274, Feb. 2016.

[16] J. Liang and W. H. Liao, “Improved design and analysis of self-powered synchronized switch interface circuit for piezoelectric energy harvesting systems,” *IEEE Trans. Ind. Electron.*, vol. 59, no. 4, pp. 1950–1960, Apr. 2012.

[17] G. Shi, Y. Xia, X. Wang, L. Qian, Y. Ye, and Q. Li, “An efficient self-powered piezoelectric energy harvesting CMOS interface circuit based on synchronous charge extraction technique,” *IEEE Trans. Circuits Syst. I, Reg. Papers*, vol. 65, no. 2, pp. 804–817, Feb. 2018.

[18] H. Xia et al., “A self-powered S-SSHI and SECE hybrid rectifier for PE energy harvesters: Analysis and experiment,” *IEEE Trans. Power Electron.*, vol. 36, no. 2, pp. 1680–1692, Feb. 2021.

[19] M. Lallart, “High gain, load-tolerant self-powered series–parallel synchronized switching technique for piezoelectric energy harvesting,” *IEEE Trans. Power Electron.*, vol. 37, no. 7, pp. 8649–8658, Jul. 2022.

[20] A. Shareef, W. L. Goh, S. Narasimalu, and Y. Gao, “A rectifier-less AC–DC interface circuit for ambient energy harvesting from low-voltage piezoelectric transducer array,” *IEEE Trans. Power Electron.*, vol. 34, no. 2, pp. 1446–1457, Feb. 2019.

[21] S. Boisseau et al., “Synchronous electric charge extraction for multiple piezoelectric energy harvesters,” in *Proc. IEEE 13th Int. New Circuits Syst. Conf.*, 2015, pp. 1–4.

[22] M. Meng, D. Wang, B. D. Truong, S. Trolier-McKinstry, S. Roundy, and M. Kiani, “A multi-beam shared-inductor reconfigurable voltage/SECE mode piezoelectric energy harvesting interface circuit,” *IEEE Trans. Biomed. Circuits Syst.*, vol. 13, no. 6, pp. 1277–1287, Dec. 2019.

[23] Z. Chen, Y. Xia, G. Shi, X. Wang, H. Xia, and Y. Ye, “Self-powered multi-input serial SSHI interface circuit with arbitrary phase difference for piezoelectric energy harvesting,” *IEEE Trans. Power Electron.*, vol. 36, no. 8, pp. 9183–9192, Aug. 2021.

[24] Z. Long, P. Li, X. Wang, B. Wang, H. S.-H. Chung, and Z. Yang, “A self-powered P-SSHI array interface for piezoelectric energy harvesters with arbitrary phase difference,” *IEEE Trans. Ind. Electron.*, vol. 69, no. 9, pp. 9155–9164, Sep. 2022.

[25] X. Wang et al., “Multi-input SECE based on buck structure for piezoelectric energy harvesting,” *IEEE Trans. Power Electron.*, vol. 36, no. 4, pp. 3638–3642, Apr. 2021.

[26] Z. Long, P. Li, J. Chen, H. S.-H. Chung, and Z. Yang, “Self-powered single-inductor rectifier-less SSHI array interface with the MPPT technique for piezoelectric energy harvesting,” *IEEE Trans. Ind. Electron.*, vol. 69, no. 10, pp. 10172–10181, Oct. 2022.

[27] K. S. Yoon, S. W. Hong, and G. H. Cho, “Double pile-up resonance energy harvesting circuit for piezoelectric and thermoelectric materials,” *IEEE J. Solid-State Circuits*, vol. 53, no. 4, pp. 1049–1060, Apr. 2018.

Jiaming Xiong received the B.E. degree in electronic information science and technology from the Liaocheng University, Liaocheng, China, in 2021, and the M.S. degree in electronic information from the Ningbo University, Ningbo, China, in 2024.

His research interests include energy harvesting systems, switching power supply design, and design of analog CMOS integrated circuits.

Yinshui Xia received the B.S. degree in physics and the M.S. degree in electronic engineering from the Hangzhou University, Zhejiang, China, in 1984 and 1991, respectively, and the Ph.D. degree in electronic engineering from the Edinburgh Napier University, Edinburgh, U.K., in 2003.

He was a Visiting Scholar with King’s College London in 1999 and then joined Edinburgh Napier University as a Research Assistant and Research Fellow from 2000 to 2005. He is currently a Professor with Faculty of Electrical Engineering and Computer Science, Ningbo University, Ningbo, China. His research interests include low-power digital circuit design, logic synthesis and optimization, system on chip design, and energy harvesting systems.

Zhidong Chen received the B.E. degree in electronic and information engineering and the M.S. degree in electronic circuit and system from the Hangzhou Dianzi University, Zhejiang, China, in 2011 and 2014, respectively, and the Ph.D. degree in micro-nano information system from the Ningbo University, Ningbo, China, in 2022.

He is currently a Lecturer with the Zhejiang Wanli University, Ningbo, China. His research interests include energy harvesting systems, sensors, and measuring technology.

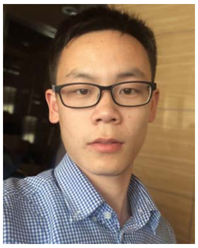

Huakang Xia received the B.E. degree in aircraft design and engineering and the Ph.D. degree in instrument science and technology from the Nanjing University of Aeronautics and Astronautics, Nanjing, China, in 2012 and 2017, respectively.

He is currently a Lecturer with Faculty of Electrical Engineering and Computer Science, Ningbo University, Ningbo, China. His current research interests include energy harvesting system, ultra-low power circuit design, as well as embedded system.

Changjian Xiao received the B.E. degree in communication engineering from the Tongling University, Tongling, China, in 2020, and the M.S. degree in electronic information from the Ningbo University, Ningbo, China, in 2024.

His research interests include energy harvesting systems and photovoltaic inverter systems.